Applied Mathematical Modelling 88 (2020) 933–950

Contents lists available at ScienceDirect

Applied Mathematical Modelling

journal homepage: www.elsevier.com/locate/apm

Stochastic semidiscretization method: Second moment stability analysis of linear stochastic periodic dynamical systems with delays

Henrik T Sykora*, Dániel Bachrathy

MTA-BME Lendület Machine Tool Vibration Research Group, Department of Applied Mechanics, Budapest University of Technology and Economics, Budapest, Hungary

ARTICLE INFO

Article history:
Received 26 December 2019
Revised 24 June 2020
Accepted 28 June 2020
Available online 5 August 2020

Keywords:
Stochastic semidiscretisation
Moment stability analysis
Stochastic delay differential equation
Periodic dynamical system
Stochastic delayed Mathieu equation
Spindle speed variation

ABSTRACT

In this paper, an efficient numerical approach is presented, which allows the analysis of the moment dynamics, stability, and stationary behavior of linear periodic stochastic delay differential equations. The method leads to a high dimensional stochastic mapping with periodic statistical properties, from which the periodic first and second moment mappings are derived. The application of the method is demonstrated first through the analysis of the stochastic delay Mathieu equation. Then a practical case study, where the effect of spindle speed variation on the stability and the resulting surface quality of turning operations is investigated.

© 2020 The Authors. Published by Elsevier Inc.
This is an open access article under the CC BY-NC-ND license.
(http://creativecommons.org/licenses/by-nc-nd/4.0/)

1. Introduction

The stability analysis of the solution of differential equations with time delay is often used in different fields of science, such as biology, where time delays are considered e.g., in predator-prey systems [1] and neural networks [2] or in engineering problems such as delay control loops [3], traffic dynamics [4] or machine tool vibrations [5]. When constructing the mathematical models describing the investigated phenomenon, the parameters have to be identified. Usually, the mean value of the measured parameters is used for the modeling, while the measured variance is considered to originate from measurement noise [6], however, it can be an inherent property of the modeled process. In case of modeling stochastic effects, a first approach is to consider them as external additive noise exciting the system, although the parameters can also change stochastically.

These variations may take the form of a stochastically changing delay [7], which can be considered as a system stochastically switching between fundamentally deterministic dynamics. There are also systems, where the parameters can be considered to behave according to a stochastic process [8]. A combination of these effects can also occur, namely, the Markovian switchings are also accompanied by noise excitation or even [9,10]. These stochastic effects are essential to include in the models since they can change the stability properties and cause unwanted oscillations, such as stochastic coherence resonance [11], that deterministic models cannot predict.

* Corresponding author.
E-mail address: bachrathy@mm.bme.hu (D. Bachrathy).

https://doi.org/10.1016/j.apm.2020.06.078
0307-904X/© 2020 The Authors. Published by Elsevier Inc. This is an open access article under the CC BY-NC-ND license.
(http://creativecommons.org/licenses/by-nc-nd/4.0/)

For example, in manufacturing science, machine tool vibrations can cause many problems, especially during roughing processes, where large material removal rate is required. There are two main categories of machine tool vibrations: the so-called chatter and forced vibrations [5]. Chatter is an instability phenomenon due to self-induced oscillations, which can lead to poor surface quality and damages the tool. This is caused by the surface regeneration effect and can be described by models with time-delay. The forced vibrations are the result of the time-varying cutting force, which can occur due to the changing size and shape of the chip, but also can be caused by high-frequency processes such as chip formation and segmentation, shockwaves, local inhomogeneities in the material properties, shear plane oscillation, rough surface of the workpiece, etc. However, these variations are usually not considered [12,13] in the constant parameters of the force characteristics describing the relationship between the chip size and the cutting force, although these excitations may significantly influence the behavior of these systems. Since these high-speed phenomena are very complex processes, thus a stochastic noise excitation is used to take the effect of these unmodeled dynamics into account [14–16].

To model machining processes, such as milling or turning operations with spindle speed variation, the use of periodic delay differential equations is necessary [17]. To decide the stability of deterministic linear periodic differential equations and to calculate the stationary periodic solution, there are well-established methods utilizing Floquet theory [18,19].

However, if the stochastic effects are also considered, the range of tools used to analyze stability and stationary solutions is far more limited than the available tools for systems described by deterministic delay differential equations (DDE's). For some special, linear stochastic delay differential equations (SDDE's) with constant parameters, stochastic calculus can be utilized to study first and second moment stability [20]. Another approach is to use small perturbation of a critical parameter to investigate the stationary properties of the selected solution of the SDDE [14,21]. In case of small delay, an alternative method is to approximate the system as a non-delayed stochastic differential equation (SDE) [22]. It is also possible to estimate the stationary probability density function (sPDF) of the phase angle in the polar-coordinate representation of the SDDE using Fokker-Planck equation [23]. This approach leads to a nonlinear deterministic system of equations for the dominant characteristic exponent, the average phase angle velocity, and the sPDF of the phase angle, which can be solved in an iterative way or by using the multidimensional bisection method [24]. There are also methods to decide, if the necessary and sufficient conditions for exponential and second moment stability are satisfied, by utilizing Lyapunov functionals [25,26]. However, the above-listed methods have the weaknesses of not only being problem-specific but usually applicable only for small degree-of-freedom dynamical systems with constant parameters.

The most general method to investigate SDDE's (including linear SDDE's with time-periodic parameters) is to numerically simulate them in the time domain using e.g., the Euler-Maruyama method [27] or the Milstein method [28,29] generalized to SDDE's, and statistically analyze the calculated trajectories to determine stability and stationary behavior. These integrated realizations then can be used to study their mean square (or in a more general case the p-th moment) to determine moment stability [30,31] and stationary behavior. A further application of these numerically obtained paths is based on data analysis, namely, the topological behavior of the high-dimensional point cloud generated from the trajectories is investigated to detect instability near the boundaries of the stable parameter domain [15,32]. Since these methods are based on Monte-Carlo simulations, they require high computational resources to provide the statistically reliable results.

In this work a different, highly efficient, general approach, that can be used for the stability analysis of a wide class of delay stochastic equations, is taken; the solution of the linearized periodic stochastic delay system is approximated with the help of the stochastic semidiscretization method [33], which results in a discrete-time periodic stochastic map. From this periodic stochastic map, the first and second moment dynamics are derived in the form of linear periodic deterministic maps: the first moment defines the mean dynamics, the second moment provides information about the average deviations around the mean dynamics. These moment mappings then are utilized to determine moment stability, which is sufficient to determine if the linear system has stationary solutions [34]. In the case of stable mappings, the stationary first and second moments are also approximated with the fixed-points of these mappings. The higher-order moment dynamics are not investigated since they do not contain additional information regarding stability [34].

This paper is organized in the following way. In Section 2, the class of the stochastic equations in question is introduced, then the discrete-time periodic map is also built up in this section. The derivation of the moment mappings of the discretized system along with the computation of the moment stability and stationary moments are discussed in Section 3. The performance and utility of this method are shown in Section 4, which is split into two main parts. In the first part, the use of periodic stochastic semidiscretization is demonstrated, and some remarks are given on its convergence properties. In the second part, the method is utilized to investigate the effect of spindle speed variation on stability and the resulting surface quality of a turning operation. Finally, conclusions are drawn in Section 5.

2. Stochastic semidiscretization of linear periodic stochastic systems

Consider the linear periodic stochastic delay differential equations (SDDE) in the incremental form:

$$\mathrm{d}\mathbf{x}_t = \big(\mathbf{A}(t)\mathbf{x}_t + \mathbf{B}(t)\mathbf{x}_{t-\tau(t)} + \mathbf{c}(t)\big)\mathrm{d}t + \big(\boldsymbol{\alpha}(t)\mathbf{x}_t + \boldsymbol{\beta}(t)\mathbf{x}_{t-\tau(t)} + \boldsymbol{\sigma}(t)\big)\mathrm{d}W_t, \tag{1}$$

where $t \mapsto \mathbf{x}_t \in \mathbb{R}^d$ is the d-dimensional state variable. $\mathbf{A}(t)$, $\mathbf{B}(t)$, $\boldsymbol{\alpha}(t)$ and $\boldsymbol{\beta}(t) \in \mathbb{R}^{d\times d}$ are periodic coefficient matrices, while $\mathbf{c}(t)$ and $\boldsymbol{\sigma}(t) \in \mathbb{R}^d$ are periodic vectors and $\tau(t) \in \mathbb{R}$ is a periodic time delay, all with with period T, namely: $\square(t) = \square(t+T)$. To differentiate the stochastic and deterministic variables, the time dependence is denoted with a subscript t (e.g.: $\mathbf{x}_t$ or W_t), or using parentheses (e.g.: $\mathbf{A}(t)$), respectively, as introduced by Arnold [34].

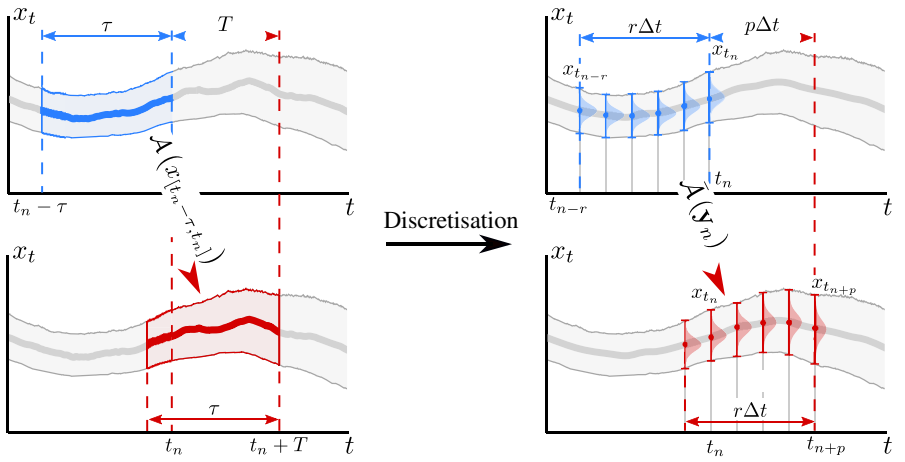

Fig. 1. Discretization of the stochastic process, where $\mathcal{A}: x_{[t_n-\tau,t_n]} \mapsto x_{[t_n+T-\tau,t_n+T]}$ represents the operator which maps the function x_t forward by a principal period T. On the right side $\bar{\mathcal{A}}: \mathbf{y}_n \mapsto \mathbf{y}_{n+p}$ represents the discretized approximation of the operator $\mathcal{A}$, which maps the discretized function x_t stored in the vector $\mathbf{y}$ with the same time period T.

To model the stochastic excitation the Wiener process $t \mapsto W_t$ is used. The Wiener increments $\mathrm{d}W_t$ follow a Gaussian distribution with expected value $\mathbb{E}(\mathrm{d}W_t) = 0$ and variation $\mathbb{E}(\mathrm{d}W_s \mathrm{d}W_t) = \mathrm{d}t \cdot \mathbb{1}(t = s)$, where the indicator function $\mathbb{1}(.)$ gives 1 or 0 if the argument is true or false, respectively. The integration of Eq. (1) is considered in the Itô sense, however, the Stratonovich definition can also be applied, since the transformation from one to the other is well defined.

In order to numerically investigate the stationary solution of the SDDE (1), the state space of the continuous functions are reduced to a discrete one (see the sketch in Fig. 1). First, the SDDE (1) is approximated by considering the delayed term constant for a sufficiently short period of time Δt:

$$\mathrm{d}\mathbf{x}_t = \left(\bar{\mathbf{A}}(n)\mathbf{x}_t + \mathbf{B}(t)\mathbf{x}_{t_{n-r(n)}} + \mathbf{c}(t)\right)\mathrm{d}t + \left(\boldsymbol{\alpha}(t)e^{\bar{\mathbf{A}}(n)(t-t_n)}\mathbf{x}_{t_n} + \boldsymbol{\beta}(t)\mathbf{x}_{t_{n-r(n)}} + \boldsymbol{\sigma}(t)\right)\mathrm{d}W_t \tag{2}$$

where $t \in [t_n, t_{n+1}]$ and $n = 0, 1, 2, \ldots$ similarly as done in [33]. The terminology semidiscretization is used here to indicate that the present state $\mathbf{x}_t$ in the drift term is not discretized [35]. Note, that the discretized time t_n here denotes the incremented time t with the constant Δt for each n (which is not stochastic in this case, despite of the subscript notation), resulting $t_n = n\Delta t$, and $T = p\Delta t$, where $p \in \mathbb{N}^+$ is the period resolution. Furthermore, the periodic coefficient matrix $\mathbf{A}(t)$ and the time dependent delay $\tau(t)$ of the original SDDE (1) has to be approximated for each discretization interval $t \in [t_n, t_{n+1}]$ by their time average over the discretization intervals:

$$\bar{\mathbf{A}}(n) = \frac{1}{\Delta t}\int_{t_n}^{t_{n+1}} \mathbf{A}(t)\mathrm{d}t, \tag{3}$$

$$\bar{\tau}(n) = \frac{1}{\Delta t}\int_{t_n}^{t_{n+1}} \tau(t)\mathrm{d}t \quad \text{and} \quad r(n) = \left\lfloor \frac{\bar{\tau}(n)}{\Delta t} \right\rfloor, \tag{4}$$

so $\bar{\mathbf{A}}(n)$ and $\bar{\tau}(n)$ are constant for each interval $[t_n, t_{n+1}]$. Moreover, the multiplicative present state in the diffusion term has to be approximated since there exists no explicit analytic solution for the general linear SDE since the matrices $\mathbf{A}(t)$ and $\boldsymbol{\alpha}(t)$ are generally not exchangeable (see details in the work of Arnold [34]). However, the approximation of the multiplicative diffusion term at the present time can be improved, if it is considered to behave similarly to the expected value of the non-delayed equation (as shown in [33]). This approach results in the linear SDE (2), where the delay and the noise from the original SDDE (1) are discretized to behave as an external excitation, dependent only on the states $\mathbf{x}_{t_n}$ and $\mathbf{x}_{t_n-\bar{\tau}(n)}$ at the beginning of each interval $t \in [t_n, t_{n+1}]$. This way the solution of the linear SDE (2) can be written explicitly for the end of each time interval $[t_n, t_{n+1}]$ as:

$$\mathbf{x}_{t_{n+1}} = (\mathbf{P}(n) + \mathbf{Q}_n)\mathbf{x}_{t_n} + (\mathbf{R}(n) + \mathbf{S}_n)\mathbf{x}_{t_{n-r(n)}} + (\mathbf{v}(n) + \mathbf{w}_n), \tag{5}$$

where

$$\mathbf{P}(n) = e^{\bar{\mathbf{A}}(n)\Delta t}, \quad \mathbf{Q}_n = \int_{t_n}^{t_{n+1}} e^{\bar{\mathbf{A}}(n)(t_{n+1}-t)}\boldsymbol{\alpha}(t)e^{\bar{\mathbf{A}}(n)(t-t_n)}\mathrm{d}W_t, \tag{6}$$

$$\mathbf{R}(n) = \int_{t_n}^{t_{n+1}} e^{\bar{\mathbf{A}}(n)(t_{n+1}-t)}\mathbf{B}(t)\mathrm{d}t, \quad \mathbf{S}_n = \int_{t_n}^{t_{n+1}} e^{\bar{\mathbf{A}}(n)(t_{n+1}-t)}\boldsymbol{\beta}(t)\mathrm{d}W_t, \tag{7}$$

$$\mathbf{v}(n) = \int_{t_n}^{t_{n+1}} e^{\bar{\mathbf{A}}(n)(t_{n+1}-t)}\mathbf{c}(t)\mathrm{d}t, \quad \mathbf{w}_n = \int_{t_n}^{t_{n+1}} e^{\bar{\mathbf{A}}(n)(t_{n+1}-t)}\boldsymbol{\sigma}(t)\mathrm{d}W_t. \tag{8}$$

In order to numerically investigate the stationary solution of the SDDE (1) the discretized state space vector $\mathbf{y}_n$ at time $t_n = n\Delta t$ is introduced (see Fig. 1):

$$\mathbf{y}_n = \begin{pmatrix} \mathbf{x}_{n\Delta t}^\top & \mathbf{x}_{(n-1)\Delta t}^\top & \dots & \mathbf{x}_{(n-r)\Delta t}^\top \end{pmatrix}^\top, \quad r = \max_{n=0,1,\dots,p-1} r(n). \tag{9}$$

This allows the solution of Eq. (5) to be written as a stochastic mapping in the form [33]

$$\mathbf{y}_{n+1} = (\mathbf{F}(n) + \mathbf{G}_n)\mathbf{y}_n + (\mathbf{f}(n) + \mathbf{g}_n), \tag{10}$$

where

$$\mathbf{F}(n) = \begin{array}{c} \begin{matrix} 1 & 2 & \dots & r(n)+1 & \dots & r & r+1 \end{matrix} \\ \begin{pmatrix} \mathbf{P}(n) & \mathbf{0} & \cdots & \mathbf{R}(n) & \cdots & \mathbf{0} & \mathbf{0} \\ \mathbf{I} & \mathbf{0} & \dots & \mathbf{0} & \cdots & \mathbf{0} & \mathbf{0} \\ \vdots & \vdots & \ddots & \ddots & \dots & \ddots & \vdots \\ \mathbf{0} & \mathbf{0} & \cdots & \cdots & \cdots & \mathbf{I} & \mathbf{0} \end{pmatrix} \end{array}, \tag{11}$$

$$\mathbf{G}_n = \begin{array}{c} \begin{matrix} 1 & 2 & \dots & r(n)+1 & \dots & r & r+1 \end{matrix} \\ \begin{pmatrix} \mathbf{Q}_n & \mathbf{0} & \cdots & \mathbf{S}_n & \cdots & \mathbf{0} & \mathbf{0} \\ \mathbf{0} & \mathbf{0} & \dots & \mathbf{0} & \cdots & \mathbf{0} & \mathbf{0} \\ \vdots & \vdots & \ddots & \ddots & \dots & \ddots & \vdots \\ \mathbf{0} & \mathbf{0} & \cdots & \cdots & \cdots & \mathbf{0} & \mathbf{0} \end{pmatrix} \end{array}, \tag{12}$$

while

$$\mathbf{f}(n) = \begin{pmatrix} \mathbf{v}(n)^\top & \mathbf{0}^\top & \dots & \mathbf{0}^\top \end{pmatrix}^\top, \quad \mathbf{g}_n = \begin{pmatrix} \mathbf{w}_n^\top & \mathbf{0}^\top & \dots & \mathbf{0}^\top \end{pmatrix}^\top. \tag{13}$$

Due to the periodic nature of the coefficients in Eq. (1) the deterministic part of mapping (10) itself is also periodic with the discrete period p:

$$\mathbf{F}(n) = \mathbf{F}(n+p) \quad \text{and} \quad \mathbf{f}(n) = \mathbf{f}(n+p), \tag{14}$$

while the stochastic coefficients $\mathbf{G}_n$ and $\mathbf{g}_n$ are periodic in distribution:

$$\mathbf{G}_n \overset{\text{dist}}{=} \mathbf{G}_{n+p} \quad \text{and} \quad \mathbf{g}_n \overset{\text{dist}}{=} \mathbf{g}_{n+p}. \tag{15}$$

This originates from their periodic statistical properties, since their elements are constructed by stochastic integrals containing the periodic functions $\boldsymbol{\alpha}(t)$, $\boldsymbol{\beta}(t)$ and $\boldsymbol{\sigma}(t)$.

To obtain a stochastic mapping for a whole time period, a whole mapping period p is considered by substituting Eq. (10) for p steps. This leads to the one-period-mapping

$$\mathbf{y}_{n+p} = \left(\overset{\curvearrowleft}{\prod_{m=0}^{p-1}} (\mathbf{F}(n+m) + \mathbf{G}_{n+m}) \right) \mathbf{y}_n + \sum_{m=0}^{p-1} \left(\mathbf{f}_{n+m}^{\text{red}} + \mathbf{g}_{n+m}^{\text{red}} \right), \tag{16}$$

where reduced additive vectors $\mathbf{f}_{n+m}^{\text{red}}$ and $\mathbf{g}_{n+m}^{\text{red}}$ are

$$\mathbf{f}_{n+m}^{\text{red}} = \left(\overset{\curvearrowleft}{\prod_{m_0=m+1}^{p-1}} (\mathbf{F}(n+m_0) + \mathbf{G}_{n+m_0}) \right) \mathbf{f}(n+m), \mathbf{g}_{n+m}^{\text{red}} = \left(\overset{\curvearrowleft}{\prod_{m_0=m+1}^{p-1}} (\mathbf{F}(n+m_0) + \mathbf{G}_{n+m_0}) \right) \mathbf{g}_{n+m}. \tag{18}$$

Note, that the one-period-mapping (16) has constant deterministic and independent and identically distributed stochastic coefficient matrices and additive vectors, furthermore, $\mathbf{f}_{n+m}^{\text{red}}$ also becomes stochastic. In case of $m = p-1$ the products in Eqs. (17) and (18) become empty products (since m_0 cannot take values), so the product is interpreted as an identity matrix $\mathbf{I}$. The symbol $\curvearrowleft$ is used to emphasize that the matrices in the products are multiplied from the left as the index increases.

There are multiple ways to utilize the stochastic one-period-mapping (16). Since the elements of the coefficient matrices are defined using stochastic Itô integrals, their joint distribution can be determined, using the fact that they form a multivariate normal distribution with zero mean and computable covariance matrix. Then this joint distribution can be used to generate random matrices for direct simulation of the trajectories or to calculate, e.g., the expected value of different quantities determined with the help of these coefficient matrices and vectors. In this paper, a different approach is taken: first, the mappings describing the first and second moment dynamics are derived, then the stability and the fixed points of these mappings are investigated. This is important in engineering applications since this gives a conservative stability criterion and ensures stationary behavior.

3. Moment stability and stationary solution of the discrete mapping

Since the one-period-mapping (16) contains the discrete approximate solution of Eq. (1) it can be utilized for an approximate moment stability investigation. To give a sufficient condition for the stochastic stability of linear stochastic differential equations, the first and second moment can be studied [34]. Furthermore, the fixed point of the moment mappings can be used to approximate the stationary first and second moment of the process defined by (1), which characterize the region where the solutions are located.

3.1. First moment of the one-period-mapping

To investigate the behavior of the first and second moment of the approximating one-period-mapping (16) the expected value operator $\langle . \rangle$ is used, which refers to the ensemble average of a process (in contrast with the time average, such as in Eqs. (3) and (4)). The first moment vector of the discretized state space is:

$$\bar{\mathbf{y}}(n) := \langle \mathbf{y}_n \rangle = \left(\langle \mathbf{x}_{n\Delta t} \rangle^\top \quad \langle \mathbf{x}_{(n-1)\Delta t} \rangle^\top \quad \dots \quad \langle \mathbf{x}_{(n-r)\Delta t} \rangle^\top \right)^\top. \tag{19}$$

The first moment mapping over a discrete period p can be obtained by taking the expected value of the stochastic one-period-mapping (16):

$$\bar{\mathbf{y}}(n+p) = \mathbf{F}^{(n,p)} \bar{\mathbf{y}}(n) + \mathbf{f}^{(n,p)}, \tag{20}$$

where

$$\mathbf{F}^{(n,p)} = \overset{\curvearrowleft}{\prod_{m=0}^{p-1}} \mathbf{F}(n+m), \tag{21}$$

$$\mathbf{f}^{(n,p)} = \sum_{m=0}^{p-1} \left(\overset{\curvearrowleft}{\prod_{m_0=m+1}^{p-1}} \mathbf{F}(n+m_0) \right) \mathbf{f}(n+m). \tag{22}$$

Note, that the matrix $\mathbf{G}_{n+m}$ and vector $\mathbf{g}_{n+m}$ are not present in Eqs. (20)–(22). Since the elements of the matrix $\mathbf{G}_{n+m}$ and vector $\mathbf{g}_{n+m}$ are constructed using stochastic Itô integrals on the interval $[t_{n+m}, t_{n+m+1}]$, they are independent of the values in y_n, which contains the states up to t_n as well as from the Itô integrals on other intervals contained in $\mathbf{G}_{n+m_0}$ and $\mathbf{g}_{n+m_0}$:

$$\langle \mathbf{G}_n \rangle = \mathbf{0}, \ \langle \mathbf{g}_n \rangle = \mathbf{0}, \quad \forall n, \tag{23}$$

$$\langle \mathbf{G}_{n+m} \mathbf{y}_n \rangle = \langle \mathbf{G}_{n+m} \rangle \langle \mathbf{y}_n \rangle = \mathbf{0}, \quad \forall m \geq 0, \tag{24}$$

$$\langle \mathbf{G}_{n+m} \mathbf{G}_n \rangle = \langle \mathbf{G}_{n+m} \rangle \langle \mathbf{G}_n \rangle = \mathbf{0}, \quad \forall m \neq 0, \tag{25}$$

$$\langle \mathbf{G}_{n+m_0} \mathbf{g}_{n+m} \rangle = \langle \mathbf{G}_{n+m_0} \rangle \langle \mathbf{g}_{n+m} \rangle = \mathbf{0}, \quad \forall m_0 \neq m. \tag{26}$$

Another approach to obtain the first moment mapping (20) is to take the expected value of a single mapping step described in Eq. (10), and then applying the resultant deterministic mapping over a discrete period p. This results in the same mapping as in Eq. (20) due to the linear nature of both the original stochastic mapping and the underlying SDDE (1). Note, that the mapping matrix $\mathbf{F}^{(n,p)}$ is the approximation of the *monodromy matrix* (or *principal matrix* of *Floquet transition matrix*) $\bar{\mathbf{\Phi}}(t_n, T)$ as in [35,36] for the first moment of SDDE (1), for which the convergence properties are analyzed [42].

The first moment stability can be characterized by the spectral radius (maximum magnitude of the eigenvalues) of the mapping matrix $\mathbf{F}^{(n,p)}$:

$$\rho\left(\mathbf{F}^{(n,p)}\right) = \max_z \left\{ \mathrm{abs}(z), \ z \in \mathbb{C} : \det\left(\mathbf{F}^{(n,p)} - z\mathbf{I}\right) = 0 \right\}, \tag{27}$$

namely if $\rho(\mathbf{F}^{(n,p)}) < 1$ the mapping is first moment stable, if $\rho(\mathbf{F}^{(n,p)}) > 1$ it is first moment unstable. Furthermore, if the mapping (20) is stable, the periodic stationary first moment ($\bar{\mathbf{y}}_{\mathrm{st}}(n) = \bar{\mathbf{y}}_{\mathrm{st}}(n+p)$) can be obtained by

$$\bar{\mathbf{y}}_{\mathrm{st}}(n) = \left(\mathbf{I} - \mathbf{F}^{(n,p)}\right)^{-1} \mathbf{f}^{(n,p)}, \tag{28}$$

which is the discrete approximation of the stationary periodic mean solution, on which the stochastic motion is superimposed. Note, that due to linearity, if the stochastic effects in Eq. (1) (the coefficients of $\mathrm{d}W_t$) are neglected, then the behavior and stability properties of the obtained deterministic system is identical to the behavior of the above described first moment.

To study the effects of stochastic perturbations on the stability of the system, the second moment stability has to be considered.

3.2. Second moment of the periodic mapping

To investigate the behavior of the second moment the symmetric second moment matrix can be defined by

$$\bar{\bar{\mathbf{Y}}}(n) := \langle \mathbf{y}_n \mathbf{y}_n^\top \rangle = \begin{pmatrix} \bar{\bar{Y}}_{11}(n) & \bar{\bar{Y}}_{12}(n) & \dots & \bar{\bar{Y}}_{1,(r+1)d}(n) \\ \bar{\bar{Y}}_{12}(n) & \bar{\bar{Y}}_{22}(n) & \dots & \bar{\bar{Y}}_{2,(r+1)d}(n) \\ \vdots & \vdots & \ddots & \vdots \\ \bar{\bar{Y}}_{1,(r+1)d}(n) & \bar{\bar{Y}}_{2,(r+1)d}(n) & \dots & \bar{\bar{Y}}_{(r+1)d,(r+1)d}(n) \end{pmatrix}, \tag{29}$$

where

$$\bar{\bar{Y}}_{ij}(n) = \bar{\bar{Y}}_{ji}(n) := \langle y_{n,i} y_{n,j} \rangle. \tag{30}$$

To investigate the second moment matrix evolution, the outer product of both sides of the stochastic mapping (10) is taken

$$\begin{aligned} \mathbf{y}_{n+1}\mathbf{y}_{n+1}^\top = {} & (\mathbf{F}(n)+\mathbf{G}_n)\mathbf{y}_n\mathbf{y}_n^\top(\mathbf{F}(n)+\mathbf{G}_n)^\top + (\mathbf{F}(n)+\mathbf{G}_n)\mathbf{y}_n(\mathbf{f}(n)+\mathbf{g}_n)^\top \\ & + (\mathbf{f}(n)+\mathbf{g}_n)\mathbf{y}_n^\top(\mathbf{F}(n)+\mathbf{G}_n)^\top + (\mathbf{f}(n)+\mathbf{g}_n)(\mathbf{f}(n)+\mathbf{g}_n)^\top, \end{aligned} \tag{31}$$

Performing the multiplications in (31) and using the properties of the stochastic integrals [37] generating the elements of $\mathbf{G}_n$ and $\mathbf{g}_n$, the expected value of the squared process mapping can be written, utilizing Einstein's notation along with (30), in the form [33]

$$\begin{aligned} \bar{\bar{Y}}_{ij}(n+1) = {} & \left(F_{il}(n)F_{jk}(n) + \langle G_{n,il}G_{n,jk}\rangle\right)\bar{\bar{Y}}_{lk}(n) + \left(\left(F_{ik}(n)f_j(n) + F_{jk}(n)f_i(n)\right)\right. \\ & \left. + \langle G_{n,ik}g_{n,j} + G_{n,jk}g_{n,i}\rangle\right)\bar{y}_k(n) + \left(f_i(n)f_j(n) + \langle g_{n,i}g_{n,j}\rangle\right). \end{aligned} \tag{32}$$

The expected values in (32) can be computed using the Itô isometry [33,37]. Instead of the matrix-to-matrix mapping representation of the second moment mapping (32), the more convenient vector-to-vector mapping is used. An efficient vector-representation of the independent elements of the second moment matrix is

$$\bar{\bar{\mathbf{y}}}(n) := \left[\bar{\bar{Y}}_{11}(n), \bar{\bar{Y}}_{22}(n), \dots, \bar{\bar{Y}}_{12}(n), \bar{\bar{Y}}_{23}(n), \dots, \bar{\bar{Y}}_{1,(r+1)d}(n)\right]^\top, \tag{33}$$

where the symmetric elements of the matrix $\bar{\bar{\mathbf{Y}}}(n)$ are only considered once. Using the above vector notation, the second moment mapping (32) can be written as

$$\bar{\bar{\mathbf{y}}}(n+1) = \mathbf{H}(n)\bar{\bar{\mathbf{y}}}(n) + \mathbf{h}(n)\bar{\mathbf{y}}(n) + \left(\dot{\bar{\mathbf{f}}}(n) + \bar{\bar{\mathbf{g}}}(n)\right), \tag{34}$$

where the coefficient matrices $\mathbf{H}(n)$, $\mathbf{h}(n)$ and vectors $\dot{\bar{\mathbf{f}}}(n)$ and $\bar{\bar{\mathbf{g}}}(n)$ are calculated using the rules defined by Eq. (32) (for further details see [33]). Due to the independence of the discrete time intervals, the periodic second moment mapping can be derived from Eq. (34) as

$$\bar{\bar{\mathbf{y}}}(n+p) = \mathbf{H}^{(n,p)}\bar{\bar{\mathbf{y}}}(n) + \overline{\mathbf{h}\bar{\mathbf{y}}}^{(n,p)} + \overline{\bar{\mathbf{f}}\bar{\mathbf{g}}}^{(n,p)}, \tag{35}$$

where

$$\mathbf{H}^{(n,p)} = \overset{\curvearrowleft}{\prod_{m=0}^{p-1}} \mathbf{H}(n+m), \tag{36}$$

$$\overline{\mathbf{h}\bar{\mathbf{y}}}^{(n,p)} = \sum_{m=0}^{p-1} \left(\overset{\curvearrowleft}{\prod_{m_0=m+1}^{p-1}} \mathbf{H}(n+m_0) \right) \mathbf{h}(n+m)\bar{\mathbf{y}}(n+m), \tag{37}$$

$$\overline{\bar{\mathbf{f}}\bar{\mathbf{g}}}^{(n,p)} = \sum_{m=0}^{p-1} \left(\overset{\curvearrowleft}{\prod_{m_0=m+1}^{p-1}} \mathbf{H}(n+m_0) \right) \left(\dot{\bar{\mathbf{f}}}(n+m) + \bar{\bar{\mathbf{g}}}(n+m)\right). \tag{38}$$

Similarly to the first moment mapping, the matrix $\mathbf{H}_{(n,p)}$ behaves as a monodromy matrix $\bar{\bar{\mathbf{\Phi}}}(t_n, T)$ for the second moment process, therefore, the stability of the second moment process can be investigated using the spectral radius $\rho(\mathbf{H}^{(n,p)})$: if $\rho(\mathbf{H}^{(n,p)}) > 1$ then the mapping is unstable, if $\rho(\mathbf{H}^{(n,p)}) < 1$ then it is stable and and has a bounded stationary solution. This periodic stationary second moment vector ($\bar{\bar{\mathbf{y}}}_{\mathrm{st}}(n) = \bar{\bar{\mathbf{y}}}_{\mathrm{st}}(n+p)$) can be determined as

$$\bar{\bar{\mathbf{y}}}_{\mathrm{st}}(n) = \left(\mathbf{I} - \mathbf{H}^{(n,p)}\right)^{-1} \left(\overline{\mathbf{h}\bar{\mathbf{y}}}_{\mathrm{st}}^{(n,p)} + \overline{\bar{\mathbf{f}}\bar{\mathbf{g}}}^{(n,p)}\right), \tag{39}$$

where

$$\bar{\mathbf{h}}\bar{\bar{\mathbf{y}}}_{\mathrm{st}}^{(n,p)} = \sum_{m=0}^{p-1}\left(\overset{\curvearrowleft}{\prod_{m_0=m+1}^{p-1}}\mathbf{H}(n+m_0)\right)\mathbf{h}(n+m)\bar{\mathbf{y}}_{\mathrm{st}}(n+m). \tag{40}$$

Note, that the first moment process $\bar{\mathbf{y}}(n)$ has to be stable ($\rho(\mathbf{F}^{(n,p)}) < 1$), in order to have a bounded stationary first moment $\bar{\mathbf{y}}_{\mathrm{st}}(n)$, which is necessary for the existence of a stationary second moment $\bar{\bar{\mathbf{y}}}_{\mathrm{st}}(n)$. However, the condition $\rho(\mathbf{H}^{(n,p)}) < 1$ for the stability of the second moment process $\bar{\bar{\mathbf{y}}}(n)$ already implies that the first moment is stable and $\rho(\mathbf{F}^{(n,p)}) < 1$ is satisfied. In case of a sufficiently large period resolution p, the stability of the first two moments of the discretized form of Eq. (1) provides enough information to decide if it has a stationary solution, and the process $\mathbf{x}_t$ stays in a bounded region of the stationary mean described by $\bar{\mathbf{y}}_{\mathrm{st}}(n)$. For this purpose, the investigation of higher-order moment stability is not necessary, since it does not provide any additional information despite the complexity of its calculation.

The described method allows the moment stability investigation of the periodic SDDE (1). The effects of the different parameters on the stability properties can be approximated using the spectral radius of the coefficient matrix $\mathbf{H}^{(n,p)}$, and stability charts can be constructed in the space of the investigated parameters. In addition, the stationary behavior can be approximately described with the use of the stationary moment vectors $\bar{\mathbf{y}}_{\mathrm{st}}(n)$ and $\bar{\bar{\mathbf{y}}}_{\mathrm{st}}(n)$ in the stable domain.

Note, that when creating the approximating SDE such as (2), instead of using only a constant $\mathbf{x}_{t_{n-r(n)}}$, the Lagrange-polynomials can be utilized [33,35] as well (as described in Appendix A) to approximate the delayed state more accurately. This leads to potentially higher-order convergence for the spectral radii of the moment mapping matrices $\mathbf{F}^{(n,p)}$, $\mathbf{H}^{(n,p)}$ and the stationary first and second moments $\bar{\mathbf{y}}_{\mathrm{st}}(n)$, $\bar{\bar{\mathbf{y}}}_{\mathrm{st}}(n)$. The use of semidiscretization method with higher-order polynomials results in the same mapping as in (10), only the elements of the mapping matrices $\mathbf{F}(n), \mathbf{G}_n$ are changed. This approach leads to the same stochastic and moment mappings as described in Eqs. (10)–(40). The details of the generation of the individual mapping matrices and their convergence properties are described in [33].

Due to the complexity of the general stochastic semidiscretization method, the above described moment mappings have been implemented as an open-source Julia package *StochasticSemiDiscretizationMethod.jl* [38]. In this package, not only the stability and stationary moment calculations with zeroth-order semidiscretization are implemented, but also the higher-order semidiscretizations can be used, and it can handle multiple delays and noise sources. This package is used to demonstrate the capabilities of the proposed method by means of the examples in the following section.

4. Case studies

In this section, the application of the stochastic semidiscretization is shown for two second-order systems. Second-order differential equations are used to describe mechanical systems, due to the first derivative being the velocity and the second-order derivative being the acceleration of the coordinate describing the motion. The first example is the stochastic extension of the delay Mathieu equation, which was used for benchmarking the deterministic semidiscretization method in [36]. A simple version of the stochastic delay Mathieu equation was introduced and tested in [32], where it was used to find topological structures in the trajectories near the critical parameters. This example contains periodic coefficient matrices, however, the delay stays constant. The second example shows how the proposed method can be utilized in manufacturing science: the effect of spindle speed variation on the surface quality is investigated during turning operations. This problem leads to an SDDE with both time-periodic delay and coefficient matrices, for which both a stability and stationary second moment investigation is provided.

4.1. Stochastic delay Mathieu equation

In this section, the moment stability and stationary moments of the stochastic delay Mathieu equation are investigated, which contains multiplicative noise in both the present and past position and present velocity along with a constant additive term. Consider the stochastic delay differential equation in the Itô sense:

$$\ddot{x}_t + a_1(1+\alpha_1\Gamma_t)\dot{x}_t + (\delta + \varepsilon\cos(\omega t))(1+\alpha_0\Gamma_t)x_t = b_0(1+\beta_0\Gamma_t)x_{t-2\pi} + \sigma\Gamma_t, \tag{41}$$

where the principal period is $T = 2\pi/\omega$, while the delay $\tau(t) \equiv 2\pi$ can be set without the loss of generality. The Gaussian white noise process is described with the help of the Langevin force Γ_t:

$$W_{t_1} - W_{t_0} = \int_{t_0}^{t_1}\Gamma_s \mathrm{d}s. \tag{42}$$

The first order incremental form of the stochastic delay Mathieu Eq. (41) can be written as

$$\mathrm{d}\mathbf{x}_t = (\mathbf{A}(t)\mathbf{x}_t + \mathbf{B}(t)\mathbf{x}_{t-2\pi})\mathrm{d}t + \left(\boldsymbol{\alpha}(t)\mathbf{x}_t + \boldsymbol{\beta}(t)\mathbf{x}_{t-2\pi} + \boldsymbol{\sigma}\right)\mathrm{d}W_t, \tag{43}$$

where

$$\mathbf{A}(t) = \begin{pmatrix} 0 & 1 \\ -(\delta+\varepsilon\cos(\omega t)) & -a_1 \end{pmatrix}, \quad \mathbf{B}(t) \equiv \begin{pmatrix} 0 & 0 \\ b_0 & 0 \end{pmatrix}, \tag{44}$$

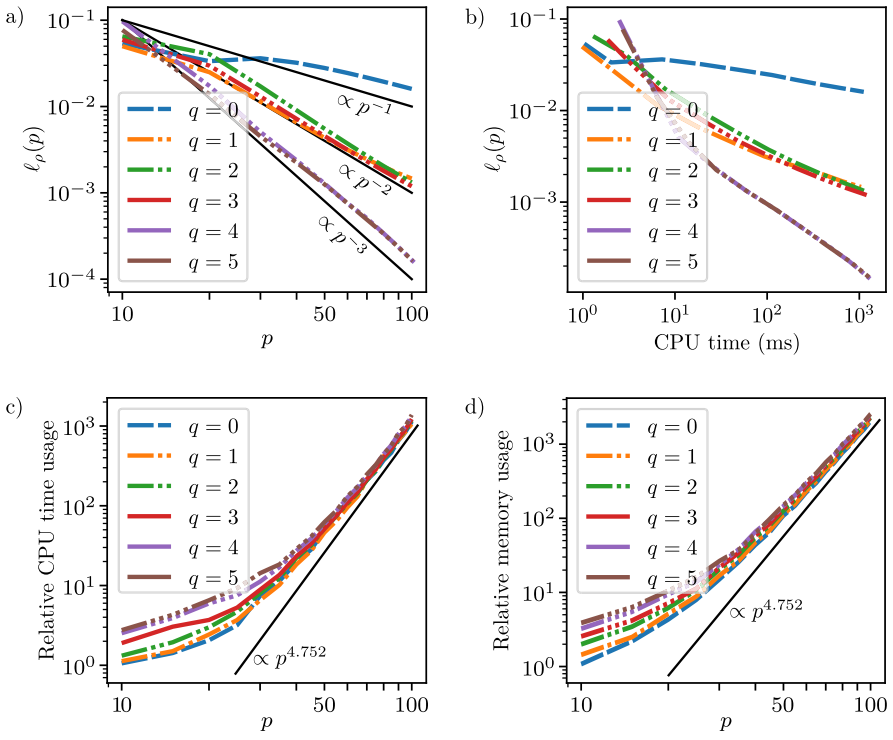

Fig. 2. Convergence properties of the spectral radius $\rho(\mathbf{H})$ with numerical parameters $a_1 = 0.2$, $\delta = 3.25$, $b_0 = -0.2$, $\sigma_0 = 0.2$, $\omega = 0.5$, $\varepsilon = 2$, $\sigma_0 = 0.2$: relative error ℓ_ρ of the spectral radius with respect to the (a) period resolution p and (b) the computational time needed, where the reference spectral radius is obtained using semidiscretization with $q = 7$ and $p_{\text{ref}} = 200$. In panels (c) and (d) the relative computation time and memory usage is shown, respectively, with reference median computation time 808.094ms and reference median memory requirement 808.59 KiB. These values correspond to $q = 0$ and $p = 10$.

$$\boldsymbol{\alpha}(t) = \begin{pmatrix} 0 & 0 \\ -\alpha_0(\delta + \varepsilon\cos(\omega t)) & -\alpha_1 a_1 \end{pmatrix}, \quad \boldsymbol{\beta}(t) = \beta_0 \mathbf{B}(t), \quad \boldsymbol{\sigma} = \begin{pmatrix} 0 \\ \sigma \end{pmatrix}. \tag{45}$$

To reduce the number of the parameters during the moment stability investigation the values of $\alpha_1, \alpha_0, \beta_0$ are set to a common value σ_0:

$$\alpha_1 \equiv \alpha_0 \equiv \beta_0 \equiv \sigma_0 \,. \tag{46}$$

To conduct numerical experiments to investigate the convergence properties of the approximation of the stability properties, the error measure ℓ_ρ is introduced:

$$\ell_\rho(\hat{p}) = \left| \frac{\rho(\mathbf{H}^{(n,p)}|_{p=\hat{p}}) - \rho(\mathbf{H}^{(n,p)}|_{p=p_{\text{ref}}})}{\rho(\mathbf{H}^{(n,p)}|_{p=p_{\text{ref}}})} \right|. \tag{47}$$

In Fig. 2 the convergence and some computational properties of the spectral radius $\rho(\mathbf{H}^{(n,p)})$ is shown through the error measure ℓ_ρ for the numerical parameters $a_1 = 0.2$, $\delta = 3.25$, $b_0 = -0.2$, $\sigma_0 = 0.2$, $\omega = 0.5$, $\varepsilon = 2$, $\sigma_0 = 0.2$ and for different q Lagrange polynomial orders. The reference solution $\rho(\mathbf{H}^{(n,p)})$ is calculated with period resolution $p_{\text{ref}} = 200$ and q =7th order Lagrange polynomial was used to approximate the delay term. In Fig. 2a the error measure ℓ_ρ is shown. To give an approximation of the convergence of ℓ_ρ, black lines are given with slopes corresponding to 1st, 2nd and 3rd order convergences. It can be observed, that the results computed with $q = 0$th order converge approximately with order 1, the results obtained using q =1st, 2nd and 3rd order semidiscretization converge approximately with order 2, while the results computed with q =4th and 5th order semidiscretization converge approximately with order 3 to the reference solution.

Furthermore, to benchmark the computational costs of the spectral radius calculation 50 sample calculations were conducted for each p and q parameter pairs and the required computational time, and the memory usage was recorded for every sample. During a benchmark sample, the whole process of the construction of the deterministic and stochastic mapping matrices, the multiplications over a mapping period, and the largest eigenvalue computation was included. The benchmarks were conducted on a workstation computer with dual Intel Xeon Gold 6154 processors and 192 GB RAM. In Fig. 2b, the error measure ℓ_ρ is shown with respect to the median of the computation time. It can be observed that if the Lagrange polynomial order q of the semidiscretization is increased, significantly higher accuracy can be achieved for the same computational time. In Fig. 2c and d, the relative time and memory required for the calculations are shown, where the reference

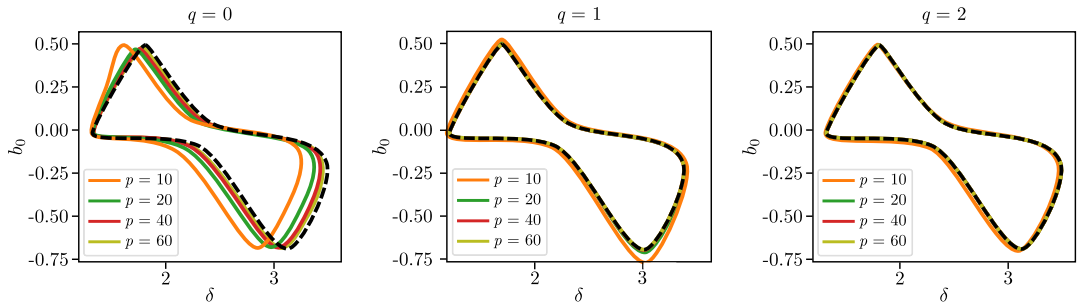

Fig. 3. Convergence of the second moment stability boundary with parameters $a_1 = 0.1$, $\omega = 1$, $\varepsilon = 1$, $\sigma_0 = 0.275$. The reference stability boundary is denoted with the dashed lines, obtained using a $q = 7$th order semidiscretization with period resolution $p = 80$.

median computation time is 808.094ms and reference median memory requirement is 808.59 KiB, which occurs at $p = 10$ and $q = 0$. Here it can be seen that the additional computation required by the higher q order semidiscretization is only significant for small p period resolutions. However, for large period resolutions p the eigenvalue computation of the sparse matrix describing $\mathbf{H}^{(n,p)}$ is the dominant source of the computational cost. Since the complexity of the eigenvalue decomposition for a matrix $\mathbf{A} \in \mathbb{R}^{n\times n}$ is approximately $\mathcal{O}(n^{2.376})$ [39,40], and the size n_H of matrix $\mathbf{H}^{(n,p)} \in \mathbb{R}^{n_H \times n_H}$ can be calculated as $n_H = \sum_{i=1}^{p} i = (p^2 + p)/2$, thus the complexity of the spectral radius calculation becomes $\mathcal{O}(p^{4.752})$. In Fig. 2c and d, this complexity can be observed in both the computational time and the memory usage for all Lagrange polynomial order q.

In Fig. 3 the convergence of the second moment stability chart is shown for the semidiscretization for different period resolutions p and Lagrange polynomial order q with parameters $a_1 = 0.1$, $\omega = 1$, $\varepsilon = 1$, $\sigma_0 = 0.275$. Since in this example the principal period $T = 2\pi/\omega$ is equal to the time delay $\tau = 2\pi$ (the frequency of the periodic term $\omega = 1$), for Lagrange polynomial order $q = 0$ and $q = 1$ the delay resolution r and period resolution p are equal, namely $r = \lfloor \tau/\Delta t + q/2 \rfloor = p$. The diagrams were constructed using a multi-dimensional bisection method [24,41] with an initial 25×16 grid for the parameters δ and b_0, respectively, followed by 5 halving iteration (the final grid is of size 800×512). As the analytical stability boundaries for this particular periodic SDDE are not known, a reference stability chart is created for the convergence analysis with $p = 80$, $q = 7$. The figure shows how the boundaries for the different approximations approach the reference boundaries denoted with the thick blue lines. It can be seen that the stability curves obtained with higher q values converge significantly better than $q = 0$ even for small period resolution p.

In Fig. 4 second moment stability charts for different parameter combinations are shown. During the calculations of these diagrams a fifth-order ($q = 5$) Lagrange polynomial was used to approximate the delay state during semidiscretization along with a sufficiently large period resolution $p = 80$. Similarly to Fig. 3 the stability boundaries were found using a multi-dimensional bisection method with an initial 25×16 grid for the parameter plane (δ, b_0) followed by 5 halving iteration. It is important to emphasize, that for cases where the time delay τ is not equal to the principal period T, the period resolution p is not equal to the delay resolution r, even in cases $q = 0$ and 1. It can be observed, that in the undamped ($a_1 = 0$) and deterministic cases (first row, blue lines for $\sigma_0 = 0$) the stability regions have a special structure, namely there are stable islands bounded by straight lines [36]. As the intensity of the stochastic terms is increased, these islands are decreasing, first only slowly near the corners, and then the stable regions completely disappear in an accelerating manner. However, if damping is added ($a_1 = 0.2$) these islands are joined, and the system described by (41) becomes much more robust against the noise. For the cases in which the ratio τ/T is not an integer (e.g., in the last row where $\tau/T = 0.5$), due to the interaction of the time-delayed term and the parametric excitation the stability charts become complex and intricate, which gets simplified as the increasing noise intensity decreases the significance of this interaction.

Note, that these robust stability boundaries are in terms of second moment stability, meaning if there is no additive noise ($\sigma = 0$) exciting the system (41), then it gives only a sufficient condition for stochastic stability (the process can be stable outside of the calculated stable domain). However, if one has to consider additive noise ($\sigma \neq 0$), then the parameters taken from the stable region calculated with this approach guarantees that the trajectories describing the solution will stay in a finitely bounded region and there exist a stationary second moment.

Next, the stationary periodic second moment determined using Eq. (39) derived from the stochastic semidiscretization method, and it is compared to results obtained with statistical evaluation of direct Monte-Carlo simulations of (41). The comparisons were conducted using the parameters $a_1 = 0.2$, $\varepsilon = 2$, $\delta = 3.25$, $b_0 = -0.2$, $\sigma_0 = 0.2$, additive noise intensity $\sigma = 1$ and three different parametric excitation frequencies: $\omega = 2, 1$ and 0.5 (denoted by black $\times$ -s in Fig. 4). The Monte-Carlo simulations were conducted using the Euler-Maruyama method for SDDE-s with time step relative to the principal period of the system $\Delta t^{MC} = T/16384 = 2\pi/16384\,\omega$. The system (41) was integrated for 1100 periods, while 200 individual trajectories were calculated. In order to ensure that the initial conditions are not influencing the results, the first 100 periods were dropped from each trajectory, leaving $1000 \times 200 = 200\,000$ periods altogether, providing statistically sufficient number of periods to average over.

The comparison is shown in Fig. 5: since the stationary first moment is zero (no additive determinist excitation is present), the convergence of the stationary periodic standard deviation is presented only. In general this is derived utilizing

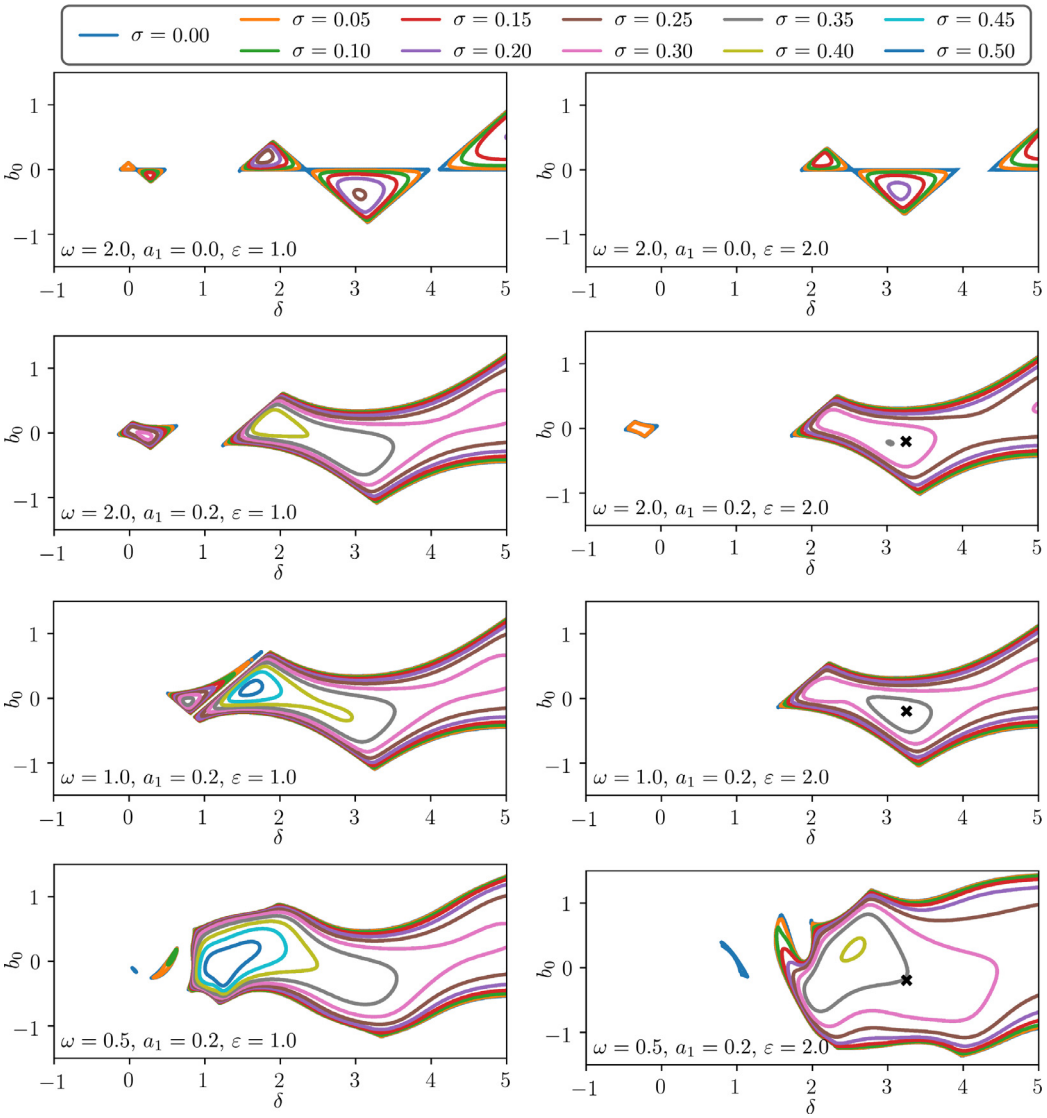

Fig. 4. Second moment stability charts for Eq. (41) for different values of ε, ω and a_1. The period resolution is $p = 80$ and the delayed state is approximated with a $q = 5$ order polynomial for all cases.

the first and second moment:

$$\mathrm{StD}(x(t)) = \sqrt{\langle x(t)^2 \rangle - \langle x(t) \rangle^2}. \tag{48}$$

Furthermore, for a more compact notation is introduced for the periodic stationary standard deviation:

$$\mathrm{StD}_x^{\mathrm{st}}(s) = \lim_{k \to \infty} \mathrm{StD}(x(kT + s)) \quad \text{where} \quad s \in [-T, 0]. \tag{49}$$

In the figure the red $\times$ -s denote the reference solution obtained via Monte-Carlo simulations, plotted with time density being $\Delta t_{\mathrm{plot}}^{MC} = T/20$. The convergence w.r.t. the period resolution p and w.r.t. the order of the Lagrange polynomial approximating the delay state q is shown in the left and right columns, respectively. When the convergence w.r.t. the period resolution p is shown, the polynomial order is fixed to $q = 0$, while when the convergence is investigated w.r.t. the order q the resolution is fixed to $p = 20$. It can be seen that the zeroth-order stochastic semidiscretization method converges to the reference solution even for smaller period resolutions ($p = 20$). However, the accuracy can be further improved if higher-order stochastic semidiscretizations are applied as it can be seen in the right column.

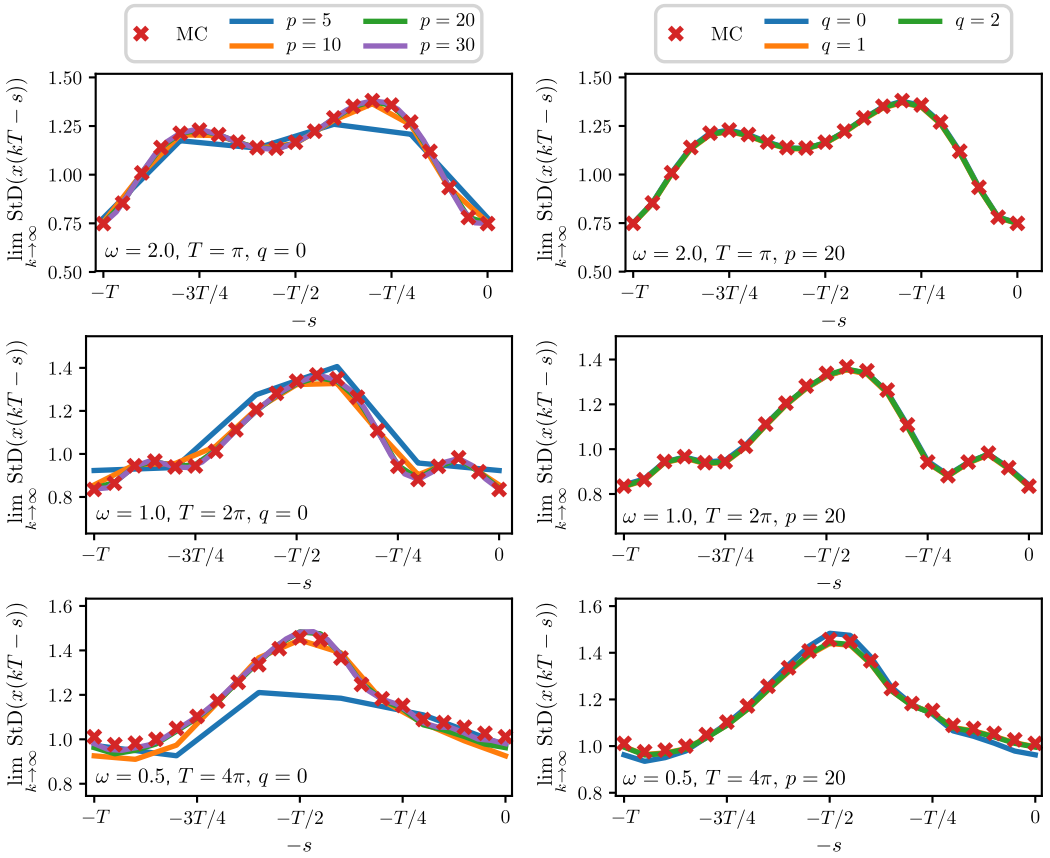

Fig. 5. Comparison of the stationary periodic standard deviations obtained with the stochastic semidiscretization method (denoted by lines) with the results obtained through Monte-Carlo simulations (denoted by the red × -s). The stationary standard deviations are calculated for different values of ω and for $a_1 = 0.2$, $\delta = 3.25$, $b_0 = -0.2$, $\sigma_0 = 0.2$ and $\varepsilon = 2$ (black × -s in Fig. 4) (For interpretation of the references to color in this figure legend, the reader is referred to the web version of this article.).

Next, to further demonstrate the convergence of the introduced stochastic semidiscretization method the mean-square error of the stationary second moment compared to a reference solution is investigated, namely

$$\ell_2(p) = \sqrt{\frac{1}{p} \sum_{t \in \Delta(p)} (\mathrm{StD}^{\mathrm{st}}_{\mathrm{x},p}(t) - \mathrm{StD}^{\mathrm{st}}_{\mathrm{x,ref}}(t))^2}, \tag{50}$$

where $\Delta(p) = \{-T, \ldots, -2T/p, -T/p\}$.

In Fig. 6a-c the $\ell_2(p)$ error is shown for period resolutions $p = 2, 4, 8, \ldots, 128$ and for $q = 0, 1, \ldots, 5$. The reference periodic stationary standard deviation was computed using a higher-order semidiscretization with $q = 7$ and $p = 256$.

To give an approximation of the convergence of the ℓ_2 error in the presented p-range black lines are given with slopes corresponding to 1st, 2nd order convergences. It can be observed that the results computed with $q = 0$th order converge approximately with order 1, the results obtained using higher-order semidiscretization converge approximately with order 2 to the reference solution. One reason for the limited convergence rate can be caused by the averaged constant $\bar{\mathbf{A}}(n)$ term in the approximating SDE (2), as similar behavior is shown for the deterministic semidiscretization in [42]. Another factor is the approximation of the multiplicative present state, which lowers the convergence rate that can be achieved even for one mapping step, as shown in [33].

Furthermore, to analyse the performance of the method to determine the stationary second moment, 50 samples of benchmark runs were conducted for each point of p and q of the stationary second moment calculation, where the required computational time and the memory usage was recorded for every sample. During a benchmark run, the whole process of the construction of the deterministic and stochastic mapping matrices and vectors, the multiplications over a mapping period, and the LU decomposition needed to solve Eq. (40) is included. In Fig. 6d and e the relative time and memory required for the calculations are shown, where the reference median computation time is 0.328 ms, and reference median memory requirement is 403.95 KiB, which occurs at $p = 10$ and $q = 0$. Here it can be seen that for large period resolutions p the matrix operations are the dominant source of the computational costs, similarly as in the case of the spectral radius calculations, demonstrated in Fig. 2c-d. Based on [43] the complexity of the LU decomposition on a parallel processor is

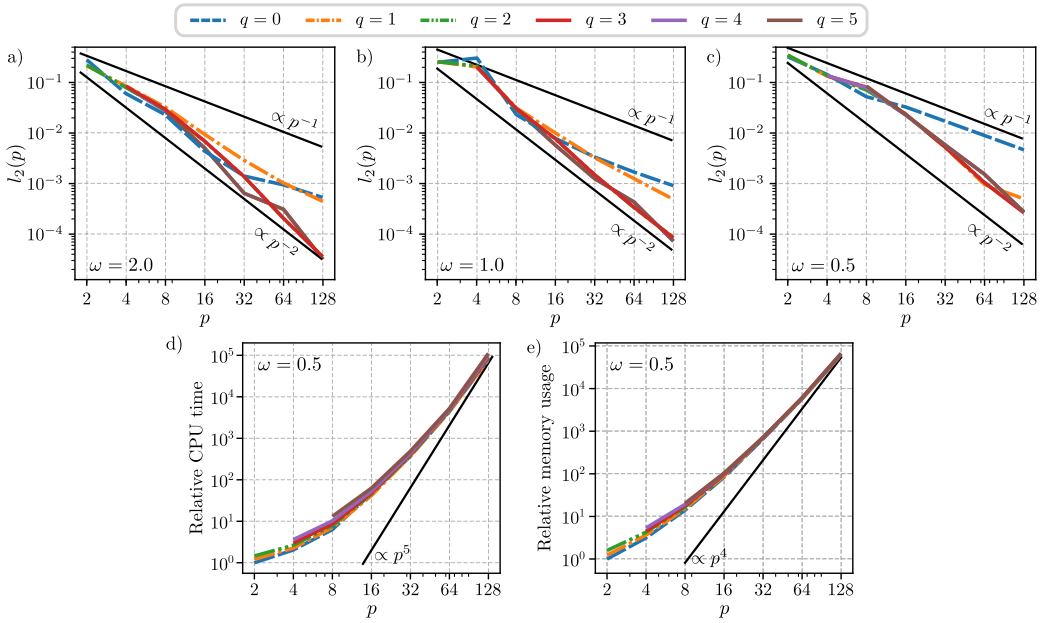

Fig. 6. Panels (a)-(c) show the $\ell_2(p)$ error defined by (50) computed utilising the stationary second moment of the stochastic delay Mathieu Eq. (41) with numerical parameters $a_1 = 0.2$, $\delta = 3.25$, $b_0 = -0.2$, $\sigma_0 = 0.2$, $\varepsilon = 2$ and $\sigma = 1$ (black $\times$ -s in Fig. 4) and reference solution computed using $q = 7$ and $p = 256$. Panels d) and e) show the median relative computation time and median memory usage of the computations, respectively, based on 50 benchmarking runs for each point. The reference median computation time is 0.328 ms, while the reference median memory requirement for the calculations is 403.95 KiB. These values correspond to $q = 0$ and $p = 2$.

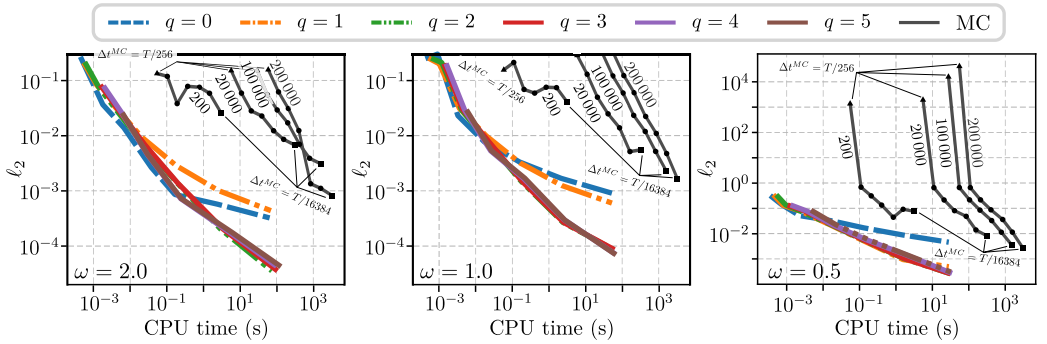

Fig. 7. The ℓ_2 error defined by (50) for the stochastic delay Mathieu equation with numerical parameters $a_1 = 0.2$, $\delta = 3.25$, $b_0 = -0.2$, $\sigma_0 = 0.2$, $\varepsilon = 2$ and $\sigma = 1$ (black $\times$ -s in Fig. 4) with respect to the required median computation time. The reference solution was computed using the stochastic semidiscretization method with $q = 7$ and $p = 256$. The results are compared to the the Monte-Carlo simulations denoted with black lines. The numbers on the black lines are corresponding to the number of the averaged periods used when statisticially evaluating the Monte-Carlo simulations.

between $\mathcal{O}(n^2)$ and $\mathcal{O}(n^3)$ for a problem of size n, so in our case it should be between $\mathcal{O}(p^4)$ and $\mathcal{O}(p^6)$. The trends observable in Fig. 6 d and e coincide with this prediction. The additional computation requirements by the higher q order semidiscretization are not significant even for small p period resolutions. Note that for higher p values, the computation of stationary quantities is challenging due to the high memory demand of the stochastic semidiscretization method ($\sim p^4$) [33].

To compare the performance of the stochastic semidiscretization method to the Monte-Carlo simulations, the computational time required for the Monte-Carlo simulations was also measured, and compared to the median computational time requirements of the stochastic semidiscretization method. In Fig. 7 the ℓ_2 error measure is shown with respect to the computational time for the stochastic semidiscretization method and for the Monte-Carlo simulations with different number of averaged periods, denoted with the numbers on the black lines and different time size $\Delta t^{\mathrm{MC}} \in \{T/2^8, T/2^9, \ldots, T/2^{14}\}$. The reference solution was calculated with stochastic semidiscretization with $q = 7$ and $p = 256$. In this figure, it can be observed that the error in the Monte-Carlo simulation is slightly influenced by the number of the averaged periods, however, the effect of the time step Δ^{MC} of the Euler-Maruyama method is the dominant factor. More importantly, it is also apparent that stochastic semidiscretization can provide the same accuracy as the Monte-Carlo simulations orders of magnitudes

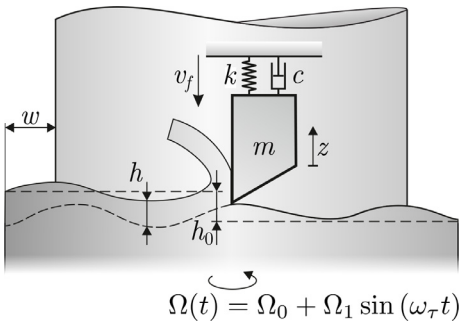

Fig. 8. One degree of freedom mechanical model of turning with periodic (sinusoidal) spindle speed variation.

faster; e.g., the stochastic semidiscretization can lead to $\ell_2 = 10^{-3}$ error using 4 magnitudes less computational resource then the applied Monte-Carlo method.

4.2. Stochastic model of turning with spindle speed variation

To demonstrate the application of the stochastic semidiscretization to a practical problem, the stability and stationary behavior of a turning operation are investigated. To improve the stability properties of the cutting process, that is to increase the domain from where stable machining parameters can be selected, and the so-called chatter [5] phenomena can be avoided, one possibility is to vary the spindle speed in a sinusoidal manner [17]. The usual mechanical model of the turning process [5] is shown in Fig. 8, while the corresponding governing equation of motion describing the dynamics is

$$m\ddot{z}(t) + c\dot{z}(t) + kz(t) = F(t), \tag{51}$$

where

$$F(t) = K\,w\,h^{q_c}(t) \quad \text{while} \quad h(t) = h_0(t) + z(t - \tau(t)) - z(t). \tag{52}$$

The system (51) models the cutting tool as a linear oscillator, which is excited by the cutting force $F(t)$ described in by the cutting force characteristics in Eq. (52) [44]. In Eq. (51) the parameters m, c and k denote the modal mass, damping and stiffness of the cutting tool, respectively, while in (52) K and q_c are parameters of the cutting force model, w is the chip width, $h(t)$ is the time varying chip thickness and $h_0(t)$ is the nominal chip thickness. The time delay $\tau(t)$ originates from the regenerative nature of turning; namely, the position of the tool is copied to the machined surface during vibration, and it affects the cutting force one revolution later through the chip thickness. The time dependence of the delay $\tau(t)$ comes from the variable spindle speed described by:

$$\Omega(t) = \Omega_0 + \Omega_1 \cos(\omega_\tau t), \quad \text{where} \quad \omega_\tau = \text{RVF} \cdot \Omega_0 \tag{53}$$

and the parameter RVF is the ratio of the modulation frequency ω_τ and the mean spindle speed Ω_0. In [35] it is shown, that the corresponding time delay $\tau(t)$ can be approximated as

$$\tau(t) \approx \tau_0 + \tau_1 \cos(\omega_\tau t), \quad \text{where} \quad \tau_0 = \frac{2\pi}{\Omega_0} \text{ and } \tau_1 = \tau_0 \cdot \text{RVA}. \tag{54}$$

Here the notation RVA $:= \Omega_1/\Omega_0$ represents the ratio of the amplitude Ω_1 and the mean value Ω_0. Due to the varying spindle speed the nominal chip thickness $h_0(t)$ varies in time, and it can be described with the help of the feed rate v_f and the varying time delay $\tau(t)$:

$$h_0(t) = v_f \tau(t), \tag{55}$$

leading to

$$F(t) = K\,w\left(v_f\tau(t) + z(t - \tau(t)) - z(t)\right)^q. \tag{56}$$

Linearizing the cutting force around $z(t - \tau(t)) - z(t) = 0$ and dividing by the modal mass m gives

$$\frac{1}{m}F(t) \approx \omega_n^2\left(H_1\left(\frac{\tau(t)}{\tau_0}\right)^{q-1}(z(t - \tau(t)) - z(t)) + H_0\left(\frac{\tau(t)}{\tau_0}\right)^q\right), \tag{57}$$

where

$$H_1 = \frac{K\,w\,q}{m\omega_n^2}\left(v_f\tau_0\right)^{q-1}, \quad H_0 = \frac{K\,w}{m\omega_n^2}\left(v_f\tau_0\right)^q \tag{58}$$

and $\omega_n = \sqrt{k/m}$ is the natural frequency.

To approximate the stochastic and high frequency effects in the cutting force [16], such as chip fragmentation, shock-waves and inhomogeneous material properties, a Gaussian white noise with relative intensity σ_K is introduced (described by the Wiener process) into the cutting force coefficient:

$$K_t := K(1+\sigma_K \Gamma_t). \tag{59}$$

When substituting it into the linearized cutting force model (57) the equation of motion becomes a SDDE:

$$\begin{aligned}
&\ddot{z}_t + 2\zeta\omega_n \dot{z}_t + \omega_n^2 z_t = \\
&= \omega_n^2 \left(H_1 \left(\frac{\tau(t)}{\tau_0} \right)^{q-1} (z_{t-\tau(t)} - z_t) + H_0 \left(\frac{\tau(t)}{\tau_0} \right)^q \right) \\
&\quad + \sigma_K \omega_n^2 \left(H_1 \left(\frac{\tau(t)}{\tau_0} \right)^{q-1} (z_{t-\tau(t)} - z_t) + H_0 \left(\frac{\tau(t)}{\tau_0} \right)^q \right) \Gamma_t,
\end{aligned} \tag{60}$$

where $\zeta = c/(2m\omega_n)$ is the damping coefficient.

To reduce the parameters of the system the dimensionless time $\hat{t} = \omega_n t$ and displacement are $x_{\hat{t}} = z_{\hat{t}}/v_f\tau_0$ are introduced. Substituting these dimensionless variables into Eq. (60) leads to

$$\begin{aligned}
&x''_{\hat{t}} + 2\zeta x'_{\hat{t}} + x_{\hat{t}} = \\
&= \left(H_1 \left(\frac{\hat{\tau}(\hat{t})}{\hat{\tau}_0} \right)^{q-1} (x_{\hat{t}-\hat{\tau}(\hat{t})} - x_{\hat{t}}) + \frac{H_1}{q} \left(\frac{\hat{\tau}(\hat{t})}{\hat{\tau}_0} \right)^q \right) \\
&\quad + \hat{\sigma}_K \left(H_1 \left(\frac{\hat{\tau}(\hat{t})}{\hat{\tau}_0} \right)^{q-1} (x_{\hat{t}-\hat{\tau}(\hat{t})} - x_{\hat{t}}) + \frac{H_1}{q} \left(\frac{\hat{\tau}(\hat{t})}{\hat{\tau}_0} \right)^q \right) \Gamma_{\hat{t}},
\end{aligned} \tag{61}$$

where

$$\hat{\tau}(t) = \hat{\tau}_0 \big(1 + \mathrm{RVA} \cos(\mathrm{RVF}\, \hat{\Omega}_0 \hat{t}) \big), \quad \text{with} \quad \hat{\Omega}_0 = \frac{\Omega_0}{\omega_n}, \quad \hat{\tau}_0 = \omega_n \tau_0 \tag{62}$$

and $\square'$ denotes the derivative w.r.t. the dimensionless time $\hat{t}$. Furthermore the coefficent $\hat{\sigma}_K := \sigma_K/\omega_n^{5/2}$ is the relative intensity of the rescaled Gaussian white noise process $\Gamma_{\hat{t}}$. For the dimensionless equation of motion (61) the coefficient matrices of the first order form (1) are given by:

$$\mathbf{A}(\hat{t}) = \begin{pmatrix} 0 & 1 \\ -1 - H_1 \left(\frac{\hat{\tau}(\hat{t})}{\hat{\tau}_0} \right)^{q-1} & -2\zeta \end{pmatrix}, \tag{63}$$

$$[6pt]\mathbf{B}(\hat{t}) = \begin{pmatrix} 0 & 0 \\ H_1 \left(\frac{\hat{\tau}(\hat{t})}{\hat{\tau}_0} \right)^{q-1} & 0 \end{pmatrix}, \quad \mathbf{c}(\hat{t}) = \begin{pmatrix} 0 \\ \frac{H_1}{q} \left(\frac{\hat{\tau}(\hat{t})}{\hat{\tau}_0} \right)^q \end{pmatrix}, \tag{64}$$

$$[6pt]\boldsymbol{\alpha}(\hat{t}) = \begin{pmatrix} 0 & 0 \\ -\hat{\sigma}_K H_1 \left(\frac{\hat{\tau}(\hat{t})}{\hat{\tau}_0} \right)^{q-1} & 0 \end{pmatrix}, \tag{65}$$

$$[6pt]\boldsymbol{\beta}(\hat{t}) = \hat{\sigma}_K \mathbf{B}(\hat{t}), \quad \boldsymbol{\sigma}(\hat{t}) = \hat{\sigma}_K \mathbf{c}(\hat{t}), \tag{66}$$

and the state space vector is

$$\mathbf{x}_{\hat{t}} = [x_{\hat{t}}, x'_{\hat{t}}]^\top. \tag{67}$$

To apply the dimensionless parameters in the Eq. (61) to investigate the effect of the spindle speed variation on the stability and the surface quality, a small number of realistic machining parameters are introduced to connect the mathematical model to the application. First, the damping ratio was set to $\zeta = 0.02$, then a cutting force model, the three-quarter rule is used, with $q_c = 3/4$ [5]. Furthermore, it is a safe assumption to consider the noise intensity in the cutting force coefficient to be $\hat{\sigma}_K = 0.1$ [16]. Another important parameter is the mean nominal chip thickness $\bar{h}_0 = v_f\tau_0$, since this scales the dimensionless tool position $x_{\hat{t}}$. In this analysis a realistic value, $h_0 = 100\,\mu$m is used.

To guarantee acceptable surface quality, the roughness profile parameter Ra is the commonly used metric, which describes the arithmetic mean value of the magnitude of the measured surface profile ordinates [45]. However, this value cannot be directly calculated using the theorem described in this paper, so the roughness parameter Rq is used, which refers to the root mean square of the surface profile ordinates. For a roughing operation it is sufficient to choose Rq 13.75,

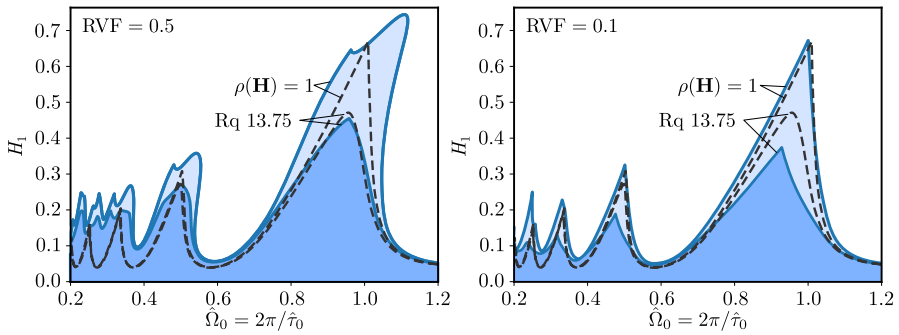

Fig. 9. Second moment stability and Rq 13.75 limiting charts for turning process with sinusoidal spindle speed modulation with RVA $= \Omega_1/\Omega_0 = 0.1$. The dashed lines indicate the corresponding boundaries associated with constant spindle speed turning. Under the curves denoted with $\rho(\mathbf{H}^{(n,p)}) = 1$ and Rq 13.75 the process is second moment stable and the maximum of the stationary standard deviation is smaller then the limit 13.75 µm, respectively.

referring to the standard deviation of the surface roughness profile peaks being at maximum 13.75 µm, which approximately corresponds to a Ra 12.5 value [46]. If $h_0 = 100\,\mu$m is chosen, then the Rq 13.75 translates to

$$\max_{s\in[-\hat{T},0]} \mathrm{StD}_x^{\mathrm{st}}(s) = 0.1375 \quad \text{where} \quad \hat{T} = \frac{2\pi}{\mathrm{RVF}\,\hat{\Omega}_0} = \frac{\hat{\tau}_0}{\mathrm{RVF}}. \tag{68}$$

To evaluate (68) one needs to calculate both the stationary first and second moments. However, the variation of the first moment is only considered in the stationary standard deviation and is not considered separately, since it does not describe the surface quality, only the final exact shape, which is not investigated in this study.

In Fig. 9 the second moment stability and the surface quality charts (where the stationary second moment is limited by the condition of Rq 13.75) are shown for modulation frequencies RVF $= \omega_\tau/\Omega_1 = 0.5$ and 0.1, while the corresponding curves for the traditional constant spindle speed turning are given with the dashed lines. The diagrams were determined using $q = 5$ order stochastic semidiscretization with period resolution $p = 50$ for all cases. The boundaries were found using a multi-dimensional bisection method with an initial 21 $\times$ 11 grid for the parameter plane of the dimensionless spindle speed $\hat{\Omega}_0$ and the dimensionless effective cutting force coefficient H_1 followed by four halving iterations, resulting in a final grid of 336 $\times$ 176.

From this analysis, it can be deduced, that the application of spindle speed variation with a relatively fast modulation frequency RVF $= 0.5$ (left panel of Fig. 9) significantly increases the stable parameter domain even for the high-speed range. This stabilizing effect is more pronounced for lower spindle speeds, where the stable "spikes" merge, creating a domain robust against uncertainty in the mean spindle speed Ω_0. This second moment stability chart is almost identical to the traditional (deterministic) stability chart [35,47], due to the relatively small noise intensity. This effect can also be observed in Fig. 4. The surface quality chart behaves similarly, the Rq 13.75 limiting curve follows the change of the stability chart for lower spindle speeds, however, higher speeds, the application of spindle speed variation with RVF $= 0.5$ does not provide any advantage.

For a more realistic frequency ratio RVF $= 0.1$ the improvement in stability is only significant in the lower spindle speed domains, as it can be observed on the right panel of Fig. 9. However, if the surface quality is also considered, the effect is not so obviously positive. Although the bottom of the "instability lobes" rise, causing increased robustness, the peak of the "spikes", inside which the preferable high material removal rates can be achieved, become significantly lower.

5. Conclusions

In this work, an efficient approach is given to determine the mean square stability and stationary second moment of stochastic delay differential equations with periodic coefficients and periodic delay. First, the stochastic semidiscretization method is extended to periodic systems subjected to additive and multiplicative noise acting both on the present and on the delayed states of the system. This allowed us to derive the periodic first and second moment mappings, then both utilized to investigate the stationary behavior of the original stochastic problem without requiring stochastic simulations. From the resulting periodic map, it is shown how the first and second moment evolution can be calculated, as well as how the stability of these moments is approximated. The periodic nature of the stationary behavior is also highlighted.

To benchmark the convergence and performance of the stochastic semidisretization on systems with periodic parameters, the method was applied for the stochastic extension of the time-periodic delay Mathieu equation. It was shown through numerical experiments that the spectral radius of the coefficient matrix $\mathbf{H}^{(n,p)}$ converges to a particular solution, either when the period resolution p or the order q of the Lagrange polynomial approximating the delayed state is increased. To elaborate, the convergence of the error ℓ_ρ of the spectral radius calculation is of order 1, 2 and 3 for the $q = 0$th order, for the $q = 1$st, 2nd, 3rd order and for the $q = 4$th, 5th order Lagrangian polynomials, respectively.

Furthermore, it was demonstrated, that it is beneficial to use a higher-order Lagrange polynomial to generate the approximating map and decrease the period resolution p to reach the same ℓ_ρ error level since the performance bottleneck of the stability calculations is the corresponding eigenvalue computation, which has the complexity $\sim \mathcal{O}(p^{4.752})$. Moreover, the effect of the intensity of the multiplicative noise on the second moment stability is explored, and it was shown that a small white noise excitation does not influence stability properties significantly, however, larger intensity noise can eliminate stable parameter regions.

Next, the convergence and the performance of the stochastic semidiscretization with respect to the stationary second moment calculation were studied through the numerical computation of the error measure ℓ_2. Similarly, to the stability calculations, both the increase of the period resolution p and the order q decreased the error ℓ_2 of the stationary second moment. Here it can also be observed that the bottleneck of the computation is the LU decomposition needed to determine the stationary behavior, thus the increased accuracy provided by the stochastic semidisretization is exceptionally beneficial. The results obtained with stochastic semidiscretization were compared to results computed with the statistical evaluation of Monte-Carlo simulations. The performance and accuracy comparison of the two methods is presented in Fig. 7, which shows the superiority of the stochastic semidiscretization method. Namely, it produced results with the same accuracy under 3-4 order of magnitudes faster than the Monte-Carlo simulations, e.g., a computation resulting in an error $\ell_2 = 10^{-3}$ for $\omega = 2.0$ is conducted ~ 0.1 s with the help of the stochastic semidiscretization. In contrast, the same accuracy is achieved under ~ 2000 s when using the Monte-Carlo approach.

Note that the error of the Monte-Carlo method is stochastic, namely, it fluctuates around a given value when repeating the calculations, while the error of the stability properties and the stationary moments computed with the help of the stochastic semidiscretization method is deterministic. Due to this deterministic property, the stability and second moment charts have smooth boundaries obtained utilizing the stochastic semidiscretization method, in contrast to the noisy and uncertain stability borders obtained with Monte-Carlo simulations [23].

Finally, the established mathematical tools were used on a practical test case: the effect of spindle speed variation on the stability of turning processes was investigated. The proposed stochastic semidiscretization allowed the efficient exploration of the stability properties of the cutting process and the resulting surface quality of the manufactured product through the stationary second moment. This analysis showed that the increased stable parameter domain does not necessarily predict a positive change in all the required quantities: in the resulting surface roughness, one can experience disadvantageous changes. This analysis emphasizes the significance of methods, which not only provide tools to analyze the stability properties of a system but also allow the evaluation of the stable stationary behavior.

Due to the complexity of the general implementation of the stochastic semidiscretization method, an open-source Julia [48] package is implemented under the name *StochasticSemiDiscretizationMethod.jl* [38]. This package allows the analysis of the first and second moment stability and the stationary periodic first and second moments of linear periodic SDDEs, by only supplying the periodic parameters of the SDDE describing the investigated problem, the period resolution p and the order q of the approximating Lagrange polynomial of the semidiscretization. Hopefully, this software package allows other researchers and practicing engineers to apply the stochastic semidiscretization in the field of stochastic delay systems.

Acknowledgments

This work was funded by the Hungarian Ministry of Human Capacities (NTP-NFT-19-B0127) and supported by the Hungarian Scientific Research Fund (OTKA FK-124462, PD-124646) and by the National Research, Development and Innovation Fund (TUDFO/51757/2019-ITM, Thematic Excellence Program).

Appendix A. Higher-order semidiscretization

To improve the accuracy and convergence of the approximation of the stochastic mapping (10), qth order Lagrange polynomials are utilized [33,35]. The term higher-order refers to the order of the Lagrange polynomial used to approximate the delayed terms. This leads to additional terms in both the deterministic and the stochastic mapping matrices. The delay resolution r is corrected with the order q of the Lagrange polynomial as

$$r(n) = \left\lfloor \frac{\overline{\tau}(n)}{\Delta t} + \frac{q}{2} \right\rfloor, \quad r = \max_{n\in\{0,1,\dots,p-1\}} r(n). \tag{A.1}$$

In this case, the Lagrange polynomial is used to approximate the delay terms, and has the following form:

$$\mathbf{L}_t^{(q)} = \sum_{k=0}^{q} L^{(q,k)}(t)\mathbf{x}_{t-(n-r(n)+k)\Delta t}\,, \tag{A.2}$$

and

$$L^{(q,k)}(t) = \left(\prod_{l=0,l\neq k}^{q} \frac{t-\overline{\tau}(n)-(n+l-r(n))\Delta t}{(k-l)\Delta t} \right) \quad \text{where} \quad t \in [t_n, t_{n+1})\,. \tag{A.3}$$

Using this, the approximation of Eq. (1) leads to

$$\mathrm{d}\mathbf{x}_t = \left(\bar{\mathbf{A}}(n)\mathbf{x}_t + \mathbf{B}(t)\,\mathbf{L}_t^{(q)} + \mathbf{c}(t)\right)\mathrm{d}t + \left(\boldsymbol{\alpha}(t)e^{\bar{\mathbf{A}}(n)s}\mathbf{x}_{t_n} + \boldsymbol{\beta}(t)\,\mathbf{L}_t^{(q)} + \boldsymbol{\sigma}(t)\right)\mathrm{d}W_t,$$
$$\text{where} \quad t \in [t_n, t_{n+1}), \tag{A.4}$$

with the discretized form

$$\mathbf{x}_{t_{n+1}} = (\mathbf{P}(n) + \mathbf{Q}_n)\mathbf{x}_{t_n} + \mathbf{v}(n) + \sum_{k=0}^{q}\left(\mathbf{R}_{\mathbf{k}}(n) + \mathbf{S}_{\mathbf{k},\mathbf{n}}\right)\mathbf{x}_{t_{n-r(n)+k}} + \mathbf{w}_n\,. \tag{A.5}$$

The discretized mapping matrices $\mathbf{F}(n)$ and $\mathbf{G}_n$ will have the structure

$$\mathbf{F}(n) = \begin{array}{c} \begin{matrix} 1 & 2 & \cdots & r(n)+q+1 & \cdots & r(n)+1 & \cdots & r & r+1 \end{matrix} \\ \begin{pmatrix} \mathbf{P}(n) & \mathbf{0} & \cdots & \mathbf{R}_q(n) & \cdots & \mathbf{R}_0(n) & \cdots & \mathbf{0} & \mathbf{0} \\ \mathbf{I} & \mathbf{0} & \cdots & \cdots & \cdots & \mathbf{0} & \cdots & \mathbf{0} & \mathbf{0} \\ \vdots & \vdots & \ddots & \ddots & \ddots & \ddots & \cdots & \vdots & \vdots \\ \mathbf{0} & \mathbf{0} & \cdots & \cdots & \cdots & \cdots & \cdots & \mathbf{I} & \mathbf{0} \end{pmatrix} \end{array}, \tag{A.6}$$

$$\mathbf{G}_n = \begin{array}{c} \begin{matrix} 1 & 2 & \cdots & r(n)+q+1 & \cdots & r(n)+1 & \cdots & r & r+1 \end{matrix} \\ \begin{pmatrix} \mathbf{Q}_n & \mathbf{0} & \cdots & \mathbf{S}_{q,n} & \cdots & \mathbf{S}_{0,n} & \cdots & \mathbf{0} & \mathbf{0} \\ \mathbf{0} & \mathbf{0} & \cdots & \cdots & \cdots & \mathbf{0} & \cdots & \mathbf{0} & \mathbf{0} \\ \vdots & \vdots & \ddots & \ddots & \ddots & \ddots & \cdots & \vdots & \vdots \\ \mathbf{0} & \mathbf{0} & \cdots & \cdots & \cdots & \cdots & \cdots & \mathbf{0} & \mathbf{0} \end{pmatrix} \end{array}, \tag{A.7}$$

where

$$\mathbf{R}_{k,n} = \int_{t_n}^{t_{n+1}} e^{\bar{\mathbf{A}}(n)(t_{n+1}-t)} L_t^{(q,k)} \mathbf{B}(s)\mathrm{d}t, \quad k = 0, 1, \ldots, q, \tag{A.8}$$

$$\mathbf{S}_{k,n} = \int_{t_n}^{t_{n+1}} e^{\bar{\mathbf{A}}(n)(t_{n+1}-t)} L_t^{(q,k)} \boldsymbol{\beta}(t)\mathrm{d}W_t\,, \quad k = 0, 1, \ldots, q. \tag{A.9}$$

Note that using the above-described approach, using a $q = 0$th order Lagrange polynomial to approximate the delayed term, the same discretization is obtained that is described in Section 2 can also be derived.

References

[1] V. Volterra, Sur la théorie mathématique des phénomènes héréditaires, J. Math. Pure Appl. 7 (1928) 149–192.
[2] S. A. Campbell, Time Delays in Neural Systems, Springer Berlin Heidelberg, Berlin, Heidelberg, pp. 65–90. doi:10.1007/978-3-540-71512-2_2.
[3] T. YaZ, The systems with delayed feedback, Avtomatika i Telemekhanika 7 (1928) 107–129.
[4] G. Orosz, R.E. Wilson, G. Stépán, Traffic jams: dynamics and control, Philosoph. Trans. R. Soc. Lond. A Math. Phys. Eng. Sci. 368 (1928) (2010) 4455–4479, doi:10.1098/rsta.2010.0205.
[5] J. Tlusty, L. Spacek, Self-excited vibrations on machine tools, Nakl. CSAV, Prague, Czech Republic, 1954.
[6] J.I. Ge, G. Orosz, Data-driven parameter estimation for optimal connected cruise control, in: Proceedings of the IEEE 56th Annual Conference on Decision and Control (CDC), IEEE, 2017, doi:10.1109/cdc.2017.8264208.
[7] M. Sadeghpour, G. Orosz, On the stability of continuous-time systems with stochastic delay: applications to gene regulatory circuitsProceedings of the 10th International Conference on Multibody Systems, Nonlinear Dynamics, and Control(46391) (2014) V006T10A078. 10.1115/DETC2014-35139
[8] G. Orosz, Traffic jam dynamics in a car-following model with reaction-time delay and stochasticity of drivers, IFAC Proc. Vol. 39 (10) (2006) 199–204, doi:10.3182/20060710-3-IT-4901.00033.
[9] R. Song, Q. Zhu, Stability of linear stochastic delay differential equations with infinite markovian switchings, Int. J. Robust Nonlinear Control 28 (3) (2018) 825–837, doi:10.1002/rnc.3905.
[10] K. Shi, J. wang, S. Zhong, Y. Tang, J. Cheng, Hybrid-driven finite-time h∞ sampling synchronization control for coupling memory complex networks with stochastic cyber attacks, Neurocomputing 387 (2020) 241–254, doi:10.1016/j.neucom.2020.01.022.
[11] R. Kuske, Competition of Noise Sources in Systems with Delay: The Role of Multiple Time Scales, J. Vibrat. Control 16 (7-8) (2010) 983–1003, doi:10.1177/1077546309341104.
[12] Y. Altintas, Manufacturing Automation: Metal Cutting Mechanics, Machine Tool Vibrations, and CNC Design, 2, Cambridge University Press, Cambridge, 2012, doi:10.1017/CBO9780511843723.
[13] J. Munoa, X. Beudaert, Z. Dombovari, Y. Altintas, E. Budak, C. Brecher, G. Stepan, Chatter suppression techniques in metal cutting, CIRP Annals 65 (2) (2016) 785–808, doi:10.1016/j.cirp.2016.06.004.
[14] E. Buckwar, R. Kuske, B. L'Esperance, T. SOO, Noise-sensitivity in machine tool vibrations, Int. J. Bifurcat. Chaos 16 (08) (2006) 2407–2416, doi:10.1142/S021812740601615X.
[15] F.A. Khasawneh, E. Munch, Chatter detection in turning using persistent homology, Mech. Syst. Signal Process. 70-71 (2016) 527–541, doi:10.1016/j.ymssp.2015.09.046.
[16] H.T. Sykora, D. Bachrathy, G. Stepan, Gaussian noise process as cutting force model for turning, Procedia CIRP 77 (2018) 94–97, doi:10.1016/j.procir.2018.08.229.
[17] T. Insperger, G. Stépán, Stability analysis of turning with periodic spindle speed modulation via semidiscretization, J. Vibrat. Control 10 (2004) 1835–1855, doi:10.1177/1077546304044891.
[18] A. Halanay, Stability theory of linear periodic systems with delay (in russian), Rev. Roum. Math. Pure A 6 (4) (1961) 633–653.
[19] J.K. Hale, S.M.V. Lunel, Introduction to Functional Differential Equations, Springer New York, 1993, doi:10.1007/978-1-4612-4342-7.

[20] M.C. Mackey, I.G. Nechaeva, Solution moment stability in stochastic differential delay equations, Phys. Rev. E 52 (4) (1995) 3366–3376, doi:10.1103/PhysRevE.52.3366.
[21] M.M. Klosek, R. Kuske, Multiscale analysis of stochastic delay differential equations, Multiscale Model. Simulat. 3 (3) (2005) 706–729, doi:10.1137/030601375.
[22] S. Guillouzic, I. L'Heureux, A. Longtin, Small delay approximation of stochastic delay differential equations, Phys. Rev. E 59 (4) (1999) 3970–3982, doi:10.1103/physreve.59.3970.
[23] H.T. Sykora, W.V. Wedig, D. Bachrathy, G. Stepan, Approximation of Top Lyapunov exponent of stochastic delayed turning model using fokker-planck approach, Proceedings of the 9th European Nonlinear Dynamics Conference (2017).
[24] D. Bachrathy, Julia package: MDBM.jl v0.1.5, Date of access: December 2019, https://github.com/bachrathyd/MDBM.jl.
[25] X. Mao, Stochastic Differential Equations and Applications, Horwood Pub, Chichester, 2008.
[26] L.E. Shaikhet, Lyapunov Functionals and Stability of Stochastic Functional Differential Equations, Springer, Cham, Switzerland New York, 2013.
[27] E. Buckwar, Introduction to the numerical analysis of stochastic delay differential equations, J. Comput. Appl. Math. 125 (1) (2000) 297–307, doi:10.1016/S0377-0427(00)00475-1. Numerical Analysis 2000. Vol. VI: Ordinary Differential Equations and Integral Equations.
[28] T. Shardlow, P. Kloeden, The milstein scheme for stochastic delay differential equations without using anticipative calculus, Stoch. Anal. Appl. 30 (2) (2012) 181–202, doi:10.1080/07362994.2012.628907.
[29] W. Cao, Z. Zhang, G.E. Karniadakis, Numerical Methods for Stochastic Delay Differential Equations Via the Wong–Zakai Approximation, SIAM J. Scient. Comput. 37 (1) (2015) A295–A318, doi:10.1137/130942024.
[30] C.T. Baker, E. Buckwar, Exponential stability in p-th mean of solutions, and of convergent euler-type solutions, of stochastic delay differential equations, J. Comput. Appl. Math. 184 (2) (2005) 404–427, doi:10.1016/j.cam.2005.01.018.
[31] X. Mao, Exponential stability of equidistant euler–maruyama approximations of stochastic differential delay equations, J. Comput. Appl. Math. 200 (1) (2007) 297–316, doi:10.1016/j.cam.2005.11.035.
[32] F.A. Khasawneh, E. Munch, Utilizing Topological Data Analysis for Studying Signals of Time-Delay Systems, Springer International Publishing, Cham, pp. 93–106. 10.1007/978-3-319-53426-8_7
[33] H.T. Sykora, D. Bachrathy, G. Stepan, Stochastic semi-discretization for linear stochastic delay differential equations, Int. J. Numer. Methods Eng. 119 (9) (2019) 879–898, doi:10.1002/nme.6076.
[34] L. Arnold, Stochastic Differential Equations: Theory and Applications, R. Oldenbourg Verlag, Munich, 1973.
[35] T. Insperger, G. Stépán, Semi-Discretization for Time-Delay Systems, Applied Mathematical Sciences, 178, Springer, New York, NY, 2011, doi:10.1007/978-1-4614-0335-7.
[36] T. Insperger, G. Stépán, Semi-discretization method for delayed systems, Int. J. Numer. Methods Eng. 55 (5) (2002) 503–518, doi:10.1002/nme.505.
[37] B. Øksendal, Stochastic Differential Equations, Springer, Berlin, Heidelberg, 2003, doi:10.1007/978-3-642-14394-6.
[38] H.T. Sykora, Julia package: StochasticSemiDiscretization.jl v0.3.3, Date of access: December 2019, https://github.com/HTSykora/StochasticSemiDiscretizationMethod.jl.
[39] D. Coppersmith, S. Winograd, Matrix multiplication via arithmetic progressions, J. Symbol. Comput. 9 (3) (1990) 251–280, doi:10.1016/s0747-7171(08)80013-2.
[40] V.Y. Pan, Z.Q. Chen, The complexity of the matrix eigenproblem, in: Proceedings of the Thirty-First Annual ACM Symposium on Theory of Computing - STOC '99, ACM Press, 1999, doi:10.1145/301250.301389.
[41] D. Bachrathy, G. Stépán, Bisection method in higher dimensions and the efficiency number, Periodica Polytechnica Mech. Eng. 56 (2) (2012) 81, doi:10.3311/pp.me.2012-2.01.
[42] T. Insperger, G. Stépán, J. Turi, On the higher-order semi-discretizations for periodic delayed systems, J. Sound Vibrat. 313 (1) (2008) 334–341, doi:10.1016/j.jsv.2007.11.040.
[43] F. Desprez, J.J. Dongarra, B. Tourancheau, Performance study of LU factorization with low communication overhead on multiprocessors, Parallel Process. Lett. 5 (1995) 157–169, doi:10.1142/S012962649500014X.
[44] Z. Dombovari, D.A. Barton, R.E. Wilson, G. Stepan, On the global dynamics of chatter in the orthogonal cuttingmodel, Int. J. Non-Linear Mech. 46 (1) (2011) 330–338, doi:10.1016/j.ijnonlinmec.2010.09.016.
[45] H. Meerkamm, Technical Pocket Guide, Shaeffler Technologies AG & Co. KG, Herzogenaurach, Germany, 2018.
[46] International Organization for Standardization, (2002) Geometrical Product Specifications (GPS) - Indication of surface texture in technical product documentation (ISO standard no.1302:2002).
[47] H.T. Sykora, D. Bachrathy, G. Stepan, A theoretical investigation of the effect of the stochasticity in the material properties on the chatter detection during turning, Proceedings of the 29th Conference on Mechanical Vibration and Noise 8 (2017).
[48] J. Bezanson, A. Edelman, S. Karpinski, V.B. Shah, Julia: A Fresh Approach to Numerical Computing, SIAM Rev. 59 (1) (2017) 65–98, doi:10.1137/141000671.